Environmental Science and Ecotechnology 30 (2026) 100677

Contents lists available at ScienceDirect

Environmental Science and Ecotechnology

journal homepage: www.journals.elsevier.com/environmental-science-and-ecotechnology/

Original Research

Morphological adaptations of cavefish support enhanced hydrodynamic perception for underwater environmental monitoring

Qi Yang [a,1], Qirui Liu [a,1], Yuling Wei [b], Chubin Weng [a], Li Ma [b], He Tian [c], Fang Zhang [d], Kenneth A. Rose [e], William R. Jeffery [f], Mengzhen Xu [a,*]

[a] State Key Laboratory of Hydroscience and Engineering, Tsinghua University, Beijing, 100084, China
[b] State Key Laboratory of Genetic Evolution & Animal Models, Kunming Institute of Zoology, Chinese Academy of Sciences, Kunming 650201, China
[c] School of Integrated Circuits, Tsinghua University, Beijing, 100084, China
[d] School of Environment, Tsinghua University, Beijing, 100084, China
[e] Horn Point Lab, University of Maryland Center for Environmental Science, Cambridge, MD, 21613, United States
[f] Department of Biology, University of Maryland, College Park, MD, 20742-4415, United States

ARTICLE INFO

Article history:
Received 5 October 2025
Received in revised form
11 February 2026
Accepted 12 February 2026

Keywords:
Environmental monitoring
Sinocyclocheilus cavefishes
Lateral line system
Hydrodynamic perception
Bio-inspired engineering
Sensors placement

ABSTRACT

Many of Earth's most biodiverse and biogeochemically active aquatic ecosystems—including groundwater karst systems, turbid estuaries and the deep ocean—are perpetually dark and hydraulically complex, making long-term, high-resolution monitoring technologically challenging. Conventional optical and acoustic sensors suffer rapid signal attenuation and high energy demand in these conditions. Cavefishes of the genus *Sinocyclocheilus*, which inhabit lightless subterranean waters, have evolved distinctive cranial morphologies—a duckbilled head, dorsal horn and hump—hypothesized to enhance hydrodynamic perception. Here we show, by combining vital staining of neuromasts with validated computational fluid dynamics simulations across a morphological series of *Sinocyclocheilus* species, that these structures dramatically amplify differential pressure signals (by up to 429.8%) and near-wall velocity gradients (by up to 69.2%) while extending perceptual range. Regions of maximal hydrodynamic variation predicted by the models closely match the observed distribution of canal and superficial neuromasts, revealing a clear biomimetic design principle: sensors should be positioned where flow-field gradients are strongest. These findings establish a quantitative, evolution-guided framework for optimizing artificial lateral line (ALL) sensor arrays, enabling autonomous underwater vehicles to perform energy-efficient, high-fidelity monitoring in some of the planet's most sensitive and data-scarce aquatic environments.

1. Introduction

A significant portion of Earth's aquatic ecosystems, from groundwater reservoirs and deep-sea habitats to turbid coastal waters, are characterized by limited light and complex flow conditions. Monitoring these environments is critical for assessing biodiversity, biogeochemical cycles, and climate impacts, but remains a formidable technological challenge [1]. Conventional sensing technologies, such as sonar and optical systems, are often hindered in these settings by high energy demands, limited operational range, and significant signal degradation [2]. An emerging alternative is to draw inspiration from nature's sensory solutions, which have been refined over millions of years of evolution to operate efficiently in challenging conditions.

In this context, the bio-inspired development of artificial lateral line (ALL) systems has garnered significant interest. Various ALL systems have been developed using velocity or pressure sensors as the primary sensing modality for underwater robots [3–7]. Recent research has focused on two main challenges: improving sensor robustness under complex flow conditions and integrating multimodal sensing to enhance environmental perception. For instance, efforts to enhance robustness address the critical challenge of distinguishing external flow signals from self-generated noise. He et al. [8] developed a magnetic deformation-based

* Corresponding author.
E-mail address: mzxu@mail.tsinghua.edu.cn (M. Xu).
[1] These authors contributed equally to the work.

https://doi.org/10.1016/j.ese.2026.100677

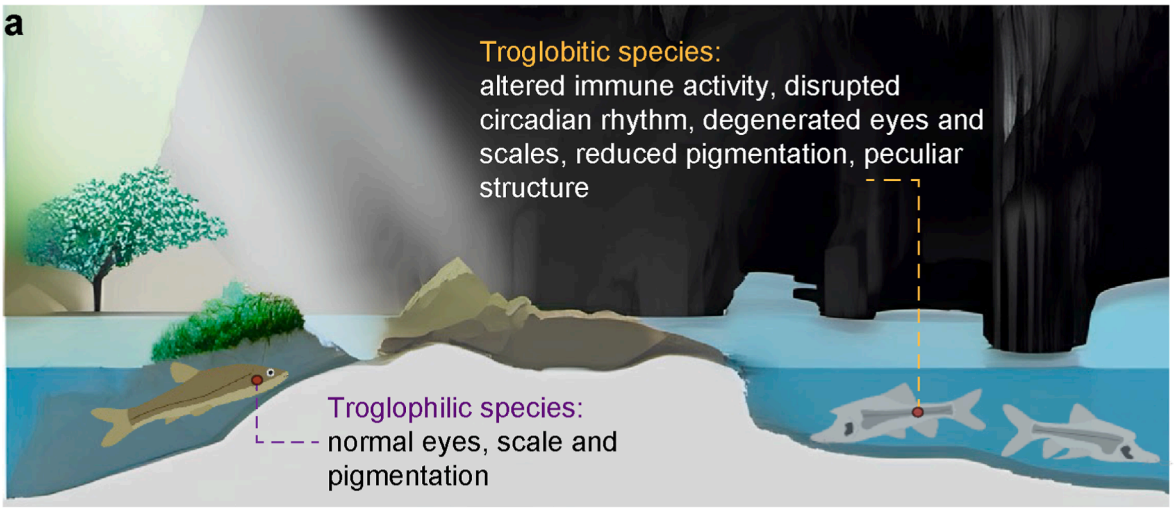
a
Troglobitic species:
altered immune activity, disrupted circadian rhythm, degenerated eyes and scales, reduced pigmentation, peculiar structure
Troglophilic species:
normal eyes, scale and pigmentation

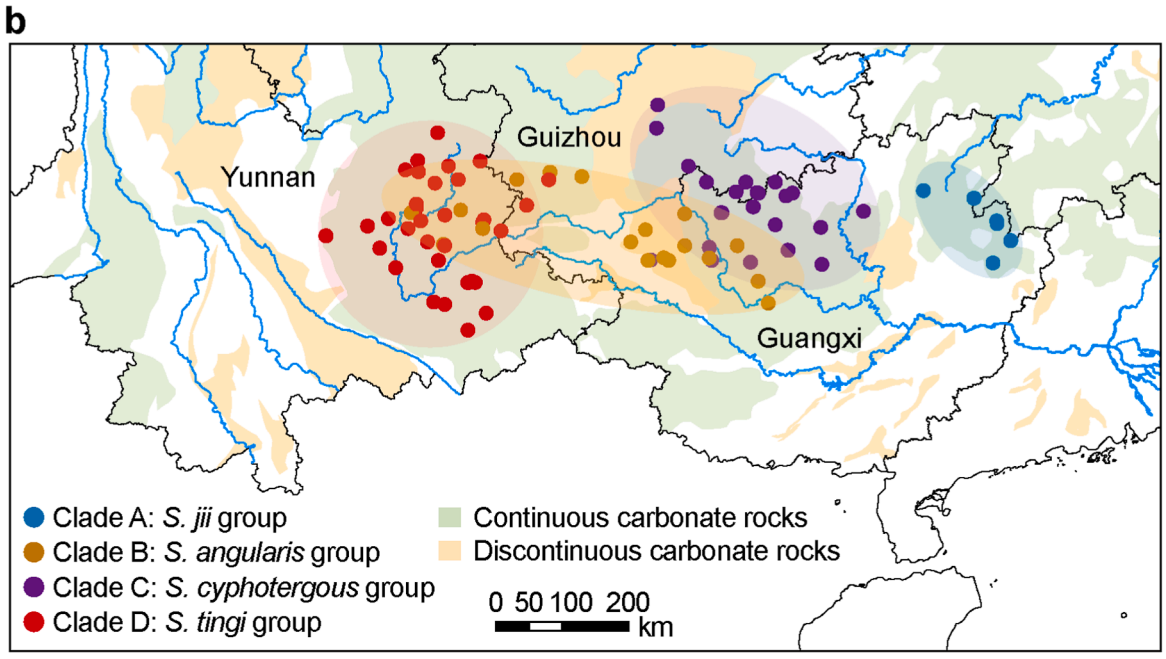
b
Yunnan
Guizhou
Guangxi
Clade A: S. jii group
Clade B: S. angularis group
Clade C: S. cyphotergous group
Clade D: S. tingi group
Continuous carbonate rocks
Discontinuous carbonate rocks
0 50 100 200
km

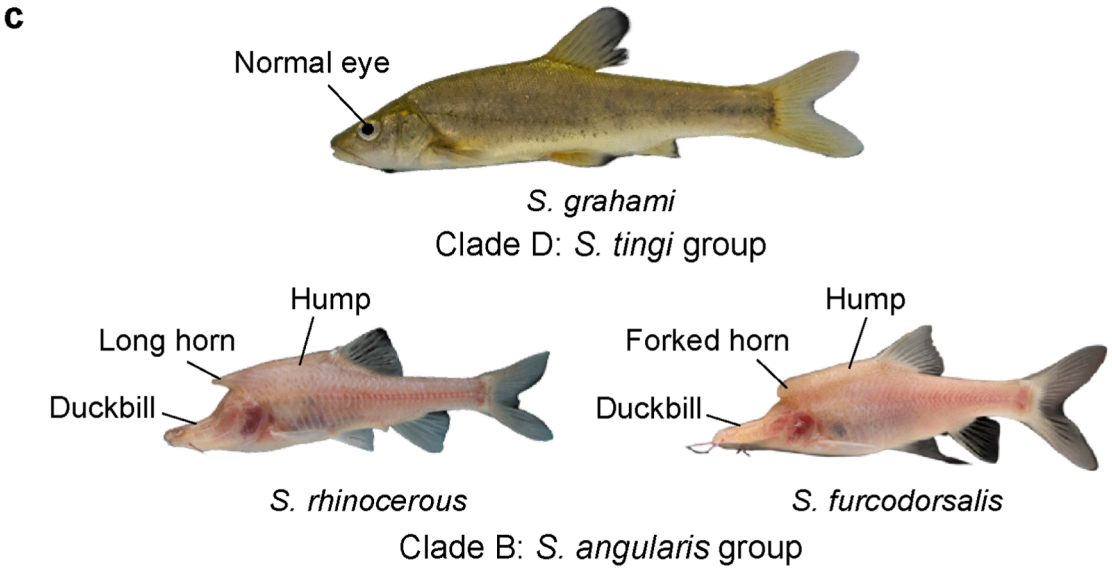
c
Normal eye
S. grahami
Clade D: S. tingi group
Hump
Long horn
Duckbill
S. rhinocerous
Hump
Forked horn
Duckbill
S. furcodorsalis
Clade B: S. angularis group

Fig. 1. Characteristics, habitats, and distribution of *Sinocyclocheilus* cavefishes. **a**, Key morphological features of troglophilic and troglobitic cavefishes in different habitats. **b**, Local distribution of *Sinocyclocheilus* species, classified into four groups, predominantly concentrated in karst areas of Yunnan, Guizhou, and Guangxi provinces. **c**, The three studied species (*S. grahami*, *S. rhinocerous*, and *S. furcodorsalis*) belong to two distinct clades with notable morphological differences, particularly in head structure (streamlined vs. duckbilled), eye degeneration, and the presence of horns and humps. The troglophilic *S. grahami* retains normal eyes and scales, whereas the troglobitic *S. rhinocerous* has reduced eyes and degenerated scales. The blind, troglobitic *S. furcodorsalis* possesses only a few scales near the lateral line.

sensor array capable of decoupling external flow measurements from disturbances caused by a robotic fish's own motion. Similarly, Zhai et al. [9] employed mode decomposition to interpret sensor signals, offering a data-driven framework for robust state estimation.

Beyond signal processing, the physical arrangement of sensors on a robotic platform presents a fundamental unsolved challenge in ALL systems design. While natural lateral line systems exhibit complex, nonuniform neuromast distributions, most artificial implementations still use simplified straight-line or uniform configurations [10–13]. A generalized, principled methodology for optimizing ALL systems sensor placement remains an open area of research. Advancements in multimodal sensing show promise; for example, Wang et al. [14] developed a fully solid-state sensor array for detecting translational moving objects with high accuracy, demonstrating robustness to variations in object shape and distance. Fu et al. [15] fused hydrodynamic and electric field sensing to improve source localization, underscoring the potential of sensor fusion. This technological gap, the lack of a principled, bio-inspired strategy for optimal sensor placement and integration, motivates a deeper investigation into biological models that have solved similar perceptual problems in nature. Here, cavefish offer a uniquely compelling model. Adapted to life in perpetually dark, low-flow aquatic caves, they represent an extreme evolutionary specialization for hydrodynamic sensing [16]. Their sophisticated lateral line system, optimized for passive perception in stagnant groundwater, offers distinct and highly relevant bio-inspiration compared to models from open-water predators such as sharks or seals. This model is directly relevant to the development of passive sensing technology for autonomous underwater vehicles (AUVs) [17,18].

Cavefish have long fascinated biologists due to their remarkable adaptations to subterranean environments, characterized by absolute darkness, frequent hypoxia, and nutrient scarcity (Fig. 1a) [19,20]. Evolution in these cave environments led to the emergence of two categories of cavefish: troglophilic and troglobitic. Troglophilic cavefish spend only part of their life cycle in caves, and thus also survive in surface waters. In contrast, troglobitic cavefish are permanently adapted to caves and exhibit distinct morphological traits that are often associated with the unique conditions of subterranean environments [16–20].

There are over 350 cavefish species, primarily found in tropical and subtropical regions (Supplementary Fig. S1), with high concentrations in the karst landscapes of Southeast Asia and Central and South America [16–22]. China boasts the highest biodiversity of cavefish species (Supplementary Fig. S1; Fig. 1b), with over 150 identified species (78 of which are troglobitic); these species are mostly in the teleost orders Cypriniformes and Siluriformes and the families Cyprinidae, Cobitidae, Nemacheilidae, and Amblycipitidae [16].

Troglobitic cavefish display a wide range of derived morphological, physiological, and behavioral features [23–31]. Morphologically, these traits include protruding jaws, modified appendages, reduced pigmentation and scales, extended barbels and fins, and distinctive features such as a dorsal horn and hump [16,19–21]. Physiologically, troglobitic cavefish are characterized by adipose storage, altered immune activity, disruptions in circadian rhythms, impaired vision, heightened sensory capacity (e.g., lateral line system) with compromised hearing, and enhanced taste receptors. Behaviorally, they show wall-following tendencies, rheotaxis, vibration attraction behavior, and modifications in schooling and foraging behavior. These unique traits make troglobitic cavefish invaluable for studying ecological adaptation to extreme environments [32–34], and they serve as ideal biological models for pioneering bio-inspired navigation and sensing systems for underwater vehicles [35–37].

Chinese cavefish, particularly those within the genus *Sinocyclocheilus* (the golden-line barbel), are prominent within the extensive karst landscape that spans approximately 620,000 km^2 of southwestern China, including eastern Yunnan, central and southern Guizhou, and northwestern Guangxi Zhuang Autonomous Region (Fig. 1b). The evolutionary history of the *Sinocyclocheilus* dates back about 10.16 million years and has been shaped by geological uplifts and climate-induced aridification that facilitated the development of cave habitats [20,38]. The distribution and differentiation of cavefish species are closely linked to specific river networks, which limit their dispersal [38]. Most *Sinocyclocheilus* species are confined to a relatively narrow geographic range, primarily within latitudes 24–27° N across the aforementioned Chinese provinces.

The genus *Sinocyclocheilus* has rapidly diversified into 76 known species, each with distinct morphological features, including elongated barbels, a duck-billed head, a horn and hump, and well-developed mechanosensory systems. Recent phylogenetic analyses classify these *Sinocyclocheilus* species into six clades, each exhibiting different body structures [39]. In general, *Sinocyclocheilus* species possess a sophisticated lateral line system with neuromast sensory units [37], categorized into superficial neuromasts (SNs) for the detection of flow and canal neuromasts (CNs) for the detection of pressure gradients [40]. Both types of neuromasts consist of sensory hair cells, supporting cells, and mantle cells, and function by detecting water motion through deflection of the cupula and bending of stereociliary bundles, leading to changes in the membrane potential of the hair cells [37]. This sensory mechanism underlies the lateral line system's role in behaviors such as rheotaxis, prey detection, predator avoidance, and social interactions. In extreme light-deprived cave environments, where visual function is greatly reduced, cavefish depend heavily on the lateral line system [40]. For instance, the vibration attraction behavior (VAB), observed in Mexican cavefish, but rarely in their surface-dwelling counterparts, improves foraging efficiency in the dark [41]. This specialized lateral line system, including more hair cells, larger canal pores, constricted canals, and heightened neural sensitivity, may enhance the ability of visually deprived cavefish to navigate, avoid predators, and surmount obstacles in darkness [21,42–44]. The evolution of distinct morphological traits has also been hypothesized to amplify the hydrodynamic stimuli detected by the lateral line system [38,45].

Although some aspects of cavefish adaptations have been studied extensively, comparative studies on their lateral line systems are limited. The most attention has been given to the Mexican blind characins (e.g., *Astyanax mexicanus*) [46–52], North American amblyopsids [53], and Brazilian cavefish [54], with some attention given to the Chinese cavefish *Sinocyclocheilus* [38,43–45,55,56]. Despite several studies attempting to elucidate the functions of the aforementioned morphological changes of

Sinocyclocheilus, their contributions in hydrodynamic sensory mechanisms, particularly in relation to lateral line neuromasts, remain unclear [21,22]. Triantafyllou et al. [57] synthesized a new paradigm for aquatic propulsion, shifting from steady-flow models to an unsteady vortex-dominated framework. This work provides the mechanistic foundation for understanding fish agility and has served as a cornerstone for the engineering of bio-inspired underwater vehicles. Shang et al. [58–60] investigated the effects of flexibility, curvature, and vibration on vortex dynamics and fluid–structure interactions. Together, these investigations offer a valuable framework for understanding how the flexibility and morphology of cavefish can alter surrounding flow patterns and enhance the detection of hydrodynamic stimuli by the lateral line system. A recent study [45] revealed how the horn structure influences hydrodynamic stimuli at the surface of *S. tianlinensis* by integrating particle image velocimetry (PIV), computational fluid dynamics (CFD), and ALL systems methodologies, significantly advancing our understanding. However, this work did not differentiate the independent functional roles of the duckbilled head, horn, and hump structures in hydrodynamic perception, nor did it explore the potential correlations between morphological adaptation and sensory function. Understanding how these structures modulate hydrodynamic stimuli is essential to translating biological principles into engineering design for enhanced environmental monitoring.

This study bridges ecology, evolutionary biology, and environmental engineering to extract bio-inspired design principles for next-generation environmental monitoring. We addressed the translational gap directly by investigating three representative *Sinocyclocheilus* species, *S. grahami*, *S. rhinocerous*, and *S. furcodorsalis*, which form a morphological series from surface-adapted to highly specialized troglobitic forms (Fig. 1c). By correlating CFD simulations of hydrodynamic stimuli with the experimentally measured distribution of lateral line neuromasts, we elucidate the functional role of the duckbilled head, horn, and hump in enhancing perception.

Our main contributions can be summarized as follows. We employed a consistent methodological approach across a model species series with absent (*S. grahami*), moderate (*S. rhinocerous*), and extreme (*S. furcodorsalis*) morphological features, allowing us to isolate the contribution of each structure. Furthermore, the virtual removal of the horn via CFD enabled us to disentangle its role from that of the duckbilled head and hump. This work provides a quantitative, bio-inspired framework to advance the design of ALL systems. By translating the link between adaptive morphology and sensory function into an engineering principle for sensor placement, we aim to enhance autonomous vehicles' ability to monitor sensitive aquatic environments where conventional sensing is challenging.

The rest of the paper is organized as follows. Section 2 describes the experimental procedures for neuromast staining and statistical analysis, as well as the computational setup for the CFD simulations, model validation, and stimulus quantification. Section 3 details the comparative distribution of neuromasts across the three *Sinocyclocheilus* species and presents a CFD analysis of enhanced hydrodynamic perception and stimulus variation. Section 4 interprets the biological and ecological implications of our findings, extends the analysis to an additional species, and elaborates on the biomimetic design principles for sensor placement in ALL systems.

2. Materials and methods

Chinese *Sinocyclocheilus* cavefish species are rare and endangered, and are classified as national second-class protected animals [16]. Due to the failure of captive breeding, obtaining embryos for genetic editing experiments is currently unfeasible, making molecular-level verification of the functions of peculiar structures impossible at this stage. To address this limitation, we employed alternative methodologies, including neuromast vital staining and CFD simulations.

2.1. Animals

Specimens of *S. grahami*, *S. rhinocerous*, and *S. furcodorsalis* ($n = 5$ per species; 15 individuals total) were obtained from captive populations within the Cavefish Evolution and Development Laboratory at the Kunming Institute of Zoology, Chinese Academy of Sciences (CAS). These specimens originated from caves in the Yunnan and Guangxi provinces of China. The average lengths for *S. grahami*, *S. rhinocerous*, and *S. furcodorsalis* were recorded as 101.7–120.0, 66.7–75.9, and 80.7–90.0 mm, respectively. The animals were maintained in glass aquaria equipped with filtration and circulation systems at a water temperature of 21 ± 1 °C. The specimens were fed specially formulated pet food, and the water in the aquaria was replaced on a weekly basis. Fish cultivation and experimental procedures adhered strictly to the guidelines set forth in protocols by Kunming, China's regulations on the ethical treatment of experimental animals and endorsed by the Kunming Institute of Zoology and CAS Animal Care and Use Committee, and the research procedures conformed to national guidelines.

The sample size ($n = 5$ per species) was constrained by the availability of these rare and protected cavefish from captive breeding populations. While limited, this sample permits robust comparative morphological and distributional analysis. Statistical approaches, including mixed-effects modeling, were employed to account for individual variations within the sample structure.

2.2. Neuromast vital staining

Neuromasts were stained with 2-(4-(dimethylamino)styryl)-1-ethylpyridinium iodide (DASPEI, Merck KGaA, Darmstadt, Germany). Each fish was individually immersed in 1 L of conditioned water containing 25 μg mL^{-1} DASPEI and kept in the dark at the maintenance temperature (21 ± 1 °C) for 2–6 h. Immediately after staining, the fish were immersed in a solution of 0.012–0.020% ethyl 3-aminobenzoate methanesulfonate salt (MS-222, Merck KGaA, Darmstadt, Germany) in conditioned water until they exhibited reduced motion and shallow breathing. Superficial and canal neuromasts were then observed using a fluorescence stereomicroscope (SteRE0 Discovery. v12, Zeiss, Jena, Germany) and a fluorescence microscope (NEXCOPE-NIB900, Ningbo, China), coupled with a computer (OptiPlex7090, Dell, Shanghai, China). High-quality images were captured using a Zeiss Axiocam CCD camera (506 color, Jena, Germany).

2.3. Statistical analysis of neuromast numbers

We compared the numbers of CNs and SNs across the three cavefish species (*S. grahami*, *S. rhinocerous*, and *S. furcodorsalis*) in six anatomical regions: anterior head, posterior trunk and tail, caudal fin, dorsal head, ventral head, and other regions (upper lateral line and dorsal fin base). Counts were recorded from multiple specimens per species, with each fish contributing data for multiple regions.

Statistical analyses were performed in MATLAB R2022b using the Statistics and Machine Learning Toolbox. To account for the repeated-measures design and control for intra-individual variability, we fitted a separate linear mixed-effects model for each region and neuromast type using the fitlme function. The model

was specified as: Count ~1 + Species + (1 | Individual_ID), where Species was treated as a fixed effect, and Individual_ID (a unique identifier for each fish–region combination) was included as a random intercept. The models were fitted under the assumption of a Gaussian distribution for the count data. Overall differences among species were evaluated using an Analysis of Variance (ANOVA) based on the fitted mixed model, with degrees of freedom approximated via the Satterthwaite method. For significant effects, planned pairwise comparisons were conducted by testing specific linear contrasts of the model coefficients with the coefTest function, corresponding to the comparisons: *S. grahami* vs. *S. rhinocerous*, *S. grahami* vs. *S. furcodorsalis*, and *S. rhinocerous* vs. *S. furcodorsalis*. Effect sizes for these pairwise differences were calculated as Cohen's *d* to quantify the magnitude of differences between species. A significance level of $p < 0.05$ was used for all tests.

2.4. Computational fluid dynamics

The hydrodynamic stimuli perceived by the lateral line system were simulated using CFD. Simulations were performed with COMSOL Multiphysics (version 6.1) using the CFD module. The Reynolds-averaged Navier–Stokes (RANS) equations were solved for steady-state, incompressible flow. This approach is well established for modeling the time-averaged flow fields around various biological shapes as it efficiently captures the dominant pressure and shear stress distributions on the body surface, the key physical signals for hydrodynamic perception [36,38,45,48]. The RANS equations, combined with the *k–ω* shear stress transport (SST) turbulence model (with a Reynolds number Re of approximately 10^4 in this study, indicating a turbulent regime), provide an efficient and accurate representation of the turbulence effects near the body of the fish, which are essential for understanding how the lateral line system detects the hydrodynamic stimuli.

The CFD modeling setup incorporated two key simplifications to focus on the sensory role of the core body morphology. First, we simulated a steady gliding state. This is a standard approach for isolating the hydrodynamic stimuli available to the lateral line system during the primary sensory phase, as validated in prior studies of hydrodynamic perception [36,38,45,48]. Second, the pectoral, pelvic, dorsal, anal, and caudal fins were omitted from the geometric models. Fins are primarily actuators for propulsion and maneuverability; their removal is a common and accepted simplification in studies analyzing the sensory modulation of body shape during passive gliding, as it minimizes confounding flow complexities from moving appendages and isolates the contribution of torso and head morphology [36,38,45,48]. While these choices simplify the absolute flow field, they are appropriate for a comparative analysis of how different body shapes modulate the baseline hydrodynamic stimulus environment.

2.4.1. Governing equations

The RANS equations are derived by decomposing the instantaneous velocity (u) and pressure (p) fields into mean (U and P) and fluctuating (u' and p') components. The RANS equations for incompressible fluid flow around cavefish are as follows [61]:

$$\frac{\partial U_i}{\partial x_i} = 0 \tag{1}$$

$$\frac{\partial \left(U_i U_j\right)}{\partial x_j} = -\frac{1}{\rho_w}\frac{\partial P}{\partial x_i} + \frac{\partial}{\partial x_j}\left(\nu \frac{\partial U_i}{\partial x_j} - \overline{u_i' u_j'}\right) \tag{2}$$

where U_i is the mean velocity component, ρ_w is the density of water, ν is the kinematic viscosity, and $-\overline{u_i' u_j'}$ is the Reynolds stress tensor, which represents the effects of turbulence and requires modeling.

2.4.2. Turbulence modeling

The SST model is a hybrid model that combines the *k–ω* model (effective near walls) and the *k–ε* model (effective in free-stream flow). It uses blending functions to smoothly transition between the *k–ω* and *k–ε* models [62].

The turbulent kinetic energy (k) equation is as follows:

$$\frac{\partial k}{\partial t} + U_j \frac{\partial k}{\partial x_j} = P_k - \beta^* \omega k + \frac{\partial}{\partial x_j}\left[\left(\nu + \sigma_k \nu_t\right)\frac{\partial k}{\partial x_j}\right] \tag{3}$$

where P_k is the production of turbulent kinetic energy, β^* is a model coefficient, ω is the specific dissipation rate, ν_t is the turbulent eddy viscosity, and σ_k is a model coefficient.

Another key equation is the specific dissipation rate (ω) equation:

$$\frac{\partial \omega}{\partial t} + U_j \frac{\partial \omega}{\partial x_j} = \alpha \frac{\omega}{k} P_k - \beta \omega^2 + \frac{\partial}{\partial x_j}\left[\left(\nu + \sigma_\omega \nu_t\right)\frac{\partial \omega}{\partial x_j}\right] + 2\left(1 - F_1\right)\frac{\sigma_{\omega 2}}{\omega}\frac{\partial k}{\partial x_i}\frac{\partial \omega}{\partial x_i} \tag{4}$$

where α, β, σ_ω, $\sigma_{\omega 2}$ are model coefficients, and F_1 is the blending function between the *k–ω* and *k–ε* models.

Turbulent eddy viscosity (ν_t) is calculated as follows:

$$\nu_t = \frac{a_1 k}{\max\left(a_1 \omega, S F_2\right)} \tag{5}$$

$$-\overline{u_i' u_j'} = -\nu_t\left(\frac{\partial U_i}{\partial j} + \frac{\partial U_j}{\partial x_i}\right) + \frac{2}{3} k \delta_{ij} \tag{6}$$

where a_1 is a model constant, S is the invariant measure of the strain rate, F_2 is another blending function, $\frac{\partial U_i}{\partial j}$ is the mean velocity gradient, and δ_{ij} is the Kronecker delta, which ensures that the diagonal terms correspond to k.

2.4.3. 3D fish body scanning

To accurately replicate the cavefish's body structure, we used a portable 3D scanner (EinScan Pro 2X 2020, Shining 3D, Hangzhou, Zhejiang, China) to generate precise geometric models. These models were refined and optimized in SolidWorks. All fins were removed from the fish's bodies, as they do not significantly impact the hydrodynamic flow during the unobstructed gliding phase of swimming.

2.4.4. Computational domain and mesh

In all simulations, the rectangular tank's dimensions measured 10 BL (body length of cavefish) in length, 10 BL in width, and 10 BL in height (Supplementary Fig. S2), containing approximately 550,000 computational cells. Within this grid, the fish geometry remained static while the flow continued to move, emulating a gliding condition. A boundary-layer mesh (inflation layer) was generated at the fish surface, with the first cell height set to achieve a target dimensionless wall distance of $y^+ \approx 30$, consistent with the resolution requirements for the applied RANS-based turbulence model. This y^+ value ensures accurate near-wall resolution for shear stress and pressure predictions relevant to lateral line stimuli.

2.4.5. Boundary conditions

A constant velocity of 1 BL s^{-1} ($Re \approx 10^4$) was uniformly applied at the inlet. A zero gradient in the normal direction was specified for each variable at the outlet, except for pressure, which was set to zero. The tank walls were assigned symmetry conditions to mimic open-water conditions and avoid boundary effects, except at the fluid–fish body interface, where a no-slip condition was applied. This condition ensures that the flow velocity at the interface remains zero (Supplementary Fig. S2 and S3).

2.4.6. Grid-independence analysis

A detailed grid-independence analysis was conducted to minimize uncertainties arising from numerical factors. This involved systematically refining the mesh and comparing key parameters (e.g., pressure) across different grid resolutions until a small variation was reached, ensuring that the results were not significantly influenced by grid size. In this study, we explored three distinct grids (coarse, medium, and fine) with varying cell resolutions to identify an optimal mesh that balances precision and computational efficiency (e.g., Supplementary Fig. S4). The mean deviation in the predicted pressure coefficient ($C_p = \frac{P}{0.5\rho_w U_\infty^2}$, where U_∞ is the free-stream velocity) between the medium and fine grids was approximately 0.09%, 1.58%, and 1.85% at $\alpha = 0°$, 10°, 15°, respectively, and the lift coefficient ($C_L = \frac{F_{lift}}{0.5\rho_w U_\infty^2}$, where F_{lift} indicates the lift force) was 0.01% (see Supplementary Table S1 for a summary of cell counts and deviations), confirming that the chosen medium grid provided a mesh-independent solution. The selected grid performed consistently over a range of varied conditions in simulations.

2.4.7. Validation of CFD model

To assess the robustness of the CFD modeling, we conducted a comprehensive set of validation tests. The model was validated by comparing its predictions with experimental data from Mateescu and Abdo [63], Lutz et al. [64], and Gregory and O'Reilly [65]. These datasets, which span Reynolds numbers from 6×10^3 to 10^6, employed similar grid structures (Supplementary Fig. S3), providing a robust basis for our validation. A finely layered mesh structure, known as an inflation layer (Supplementary Fig. S2 and S3), was employed around the airfoil to accurately resolve the boundary layer. This approach ensures a smooth transition in grid spacing near the wall, which is crucial for capturing surface aerodynamic phenomena [66]. Specifically, the validations pertained to the aerodynamic flow around an aerofoil using the NACA0008, NACA0009, and NACA0012 models with different chord lengths, and to the rotation of the angle of attack about the aerofoil's midchord. The detailed parameters employed in the three sets of wind-tunnel experiments are outlined in Supplementary Table S2. The C_p on the airfoil surfaces, along with the corresponding absolute deviations from our current model (Supplementary Fig. S4 and S5), showed satisfactory agreement with the experimental measurements. The mean deviations for the three datasets (Mateescu and Abdo [63], Lutz et al. [64], and Gregory and O'Reilly [65]) were 0.0034, 0.0241, and 0.0795, respectively. This agreement underscores the reliability and precision of our numerical model, thus rendering it an authoritative tool for subsequent inquiries.

2.4.8. Design of CFD simulations

According to previous studies [48,67,68], wall shear stress (τ_w) serves as a reliable approximation of the stimulus magnitude for superficial neuromasts, as it is proportional to the velocity difference between the fish's surface and the surrounding fluid. Therefore, we considered pressure difference and wall shear stress as key indicators of stimuli for canal and superficial neuromasts, respectively.

Following prior research [36,45,48,69], we simulated cavefish gliding in open water by maintaining fixed fish geometry in a steady-state flow. To further investigate the effects of morphology on hydrodynamic stimuli, we conducted yaw angle tests, exposing cavefish to flow attack angles of up to 30°, in line with Ristroph et al. [69] and Yang et al. [36]. We then analyzed the normalized hydrodynamic stimuli using the kinetic energy per unit volume, expressed as the differential pressure coefficient (ΔC_p) and the skin friction coefficient (C_f), almost along the real lateral line of the cavefish's body from head to tail.

Additionally, we integrated the total stress on the cavefish surface in the drag direction, represented by the drag coefficient (C_d), to assess how the morphological traits of troglobitic species influence flow resistance and swimming modes. This investigation aimed to elucidate the role of specialized morphological changes in modulating hydrodynamic interactions in troglobitic cavefish.

$$C_d = \frac{F_{drag}}{0.5\rho_w U_\infty^2 A} \tag{7}$$

$$C_p = \frac{P_i}{0.5\rho_w U_\infty^2} \tag{8}$$

$$C_f = \frac{\tau_w}{0.5\rho_w U_\infty^2} \tag{9}$$

$$\Delta C_p = \frac{P_i - P_{i+1}}{0.5\rho_w U_\infty^2} \tag{10}$$

where C_d, C_p, and C_f denote the drag, pressure, and skin friction coefficient, respectively; F_{drag}, P_i, and τ_w indicate the drag force, static pressure at the ith canal pore, and wall shear stress imposed on the cavefish surface; A is the characteristic frontal area of the cavefish body; and ΔC_p represents the difference of C_p between two adjacent canal pores i and $i+1$.

Similar to the approach used to investigate the maximum hydrodynamic stimuli on *S. tianlinensis* by Yang et al. [36], we adopted the methodology to detect the remarkable variation in hydrodynamic stimuli based on the yaw (Supplementary Fig. S2). We defined a pressure-asymmetry metric, $dp = P_{left} - P_{right}$, to capture left–right differences that fish may use to detect flow changes [36,48,69]. Using the model outputs, we then calculated the changes in pressure (Δdp, equation (11)) and wall shear stress ($\Delta\ \tau_w$, equation (12)), between adjacent angles of attack, α (for example, the difference between the results at $\alpha = 5°$ and $\alpha = 0°$, denoted 5–0°). We then merged the regions corresponding to significant stimulus variation to verify the consistency between the distribution of biological neuromasts and the regions with notable stimulus variation.

$$\Delta dp = dp_j - dp_{j-5°} \tag{11}$$

$$\Delta\tau_w = \tau_{wj} - \tau_{wj-5°} \tag{12}$$

where Δdp and $\Delta\tau_w$ indicate the changes in hydrodynamic stimuli between two attack angles of flow with the index of $j = 5°$, 10°, 15°, 20°, 25°, and 30°.

Differences were computed between consecutive angles of attack (0–30°) during steady gliding in open water at Re ≈ 104.

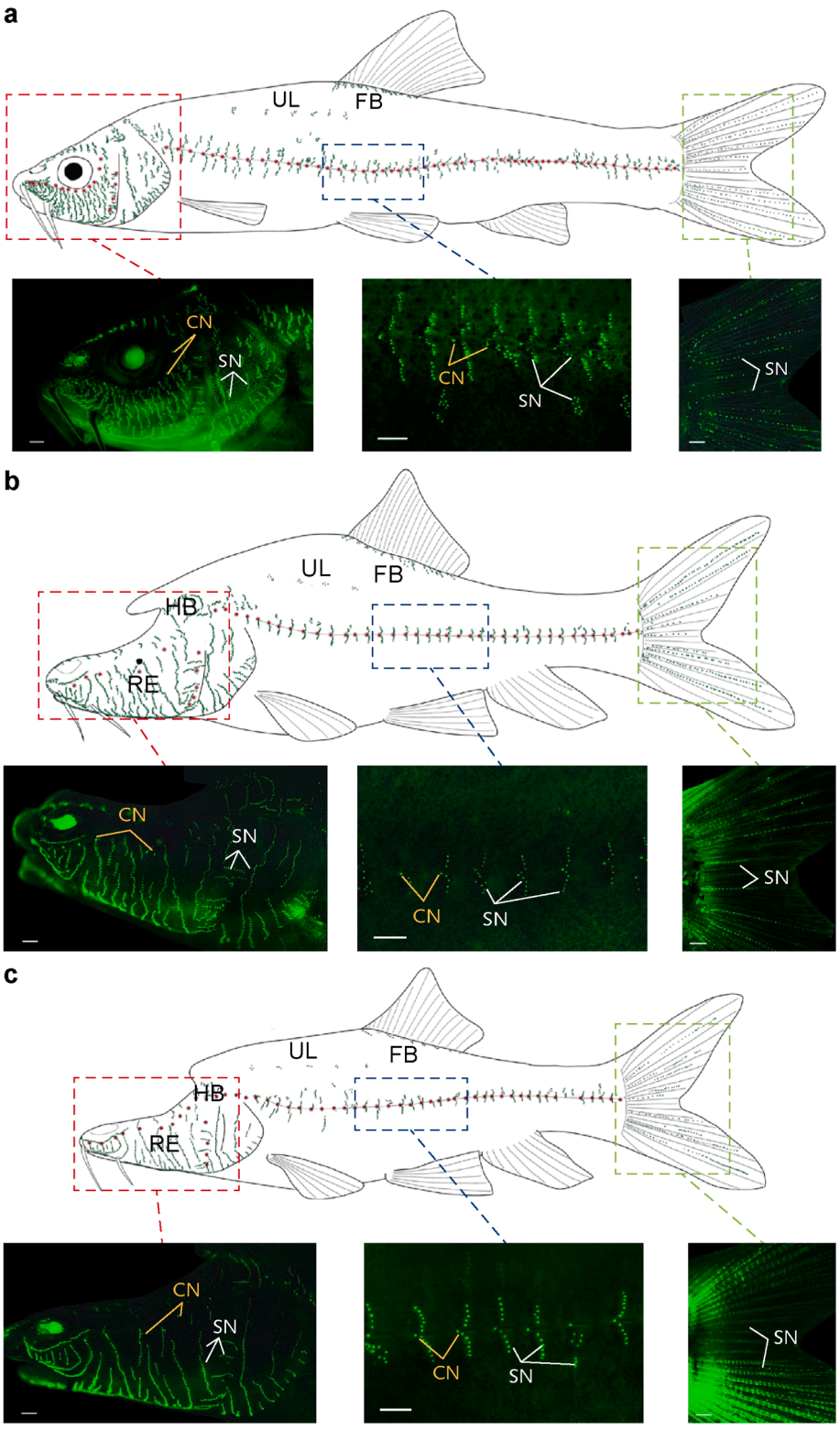

Fig. 2. Neuromast distribution in *Sinocyclocheilus* species: *S. grahami* (**a**), *S. rhinocerous* (**b**), and *S. furcodorsalis* (**c**). Top, schematic maps of superficial neuromasts (SNs; green dots) and canal neuromasts (CNs; red dots) along the head and body. RE: regressive eye; HB: the bottom edge of the horn; UL: upper lateral line; FB: dorsal fin base. Bottom: fluorescence vital staining of neuromasts in the three species. The left, middle, and right frames show drawings of real neuromast distributions in the head, trunk, and tail fin (regions boxed in the corresponding schematics; head, red; trunk, blue; caudal fin, green), where clusters of small dots represent SNs, whereas larger dot indicates CNs. Scale bar: 1 mm.

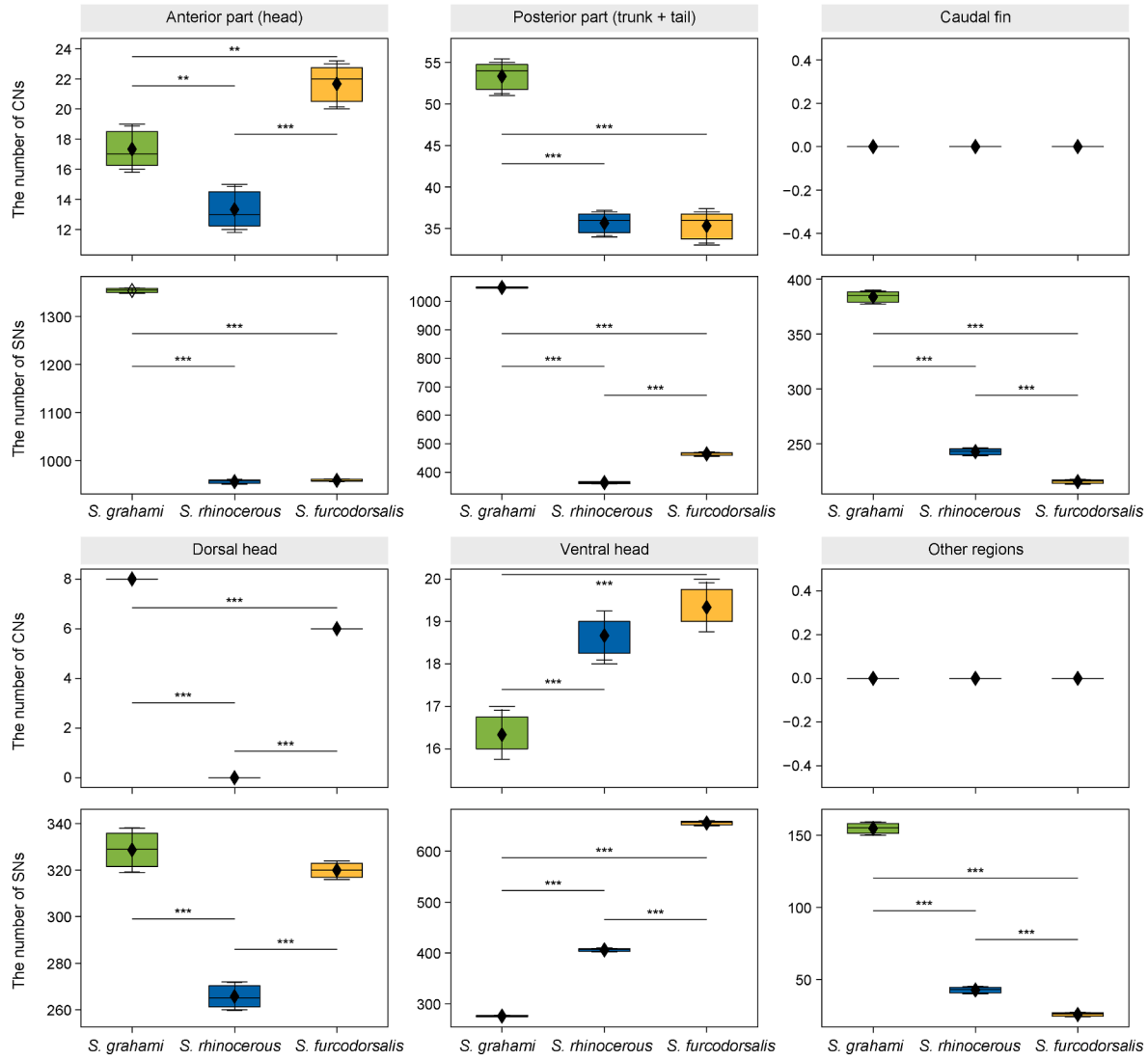

Fig. 3. Number of neuromasts distributed on cavefishes in different regions. CN: canal neuromast; SN: superficial neuromast. For each species-region combination, boxplots display the median and interquartile range. Superimposed black diamonds represent the group mean, and error bars indicate ±1 standard deviation. Note that asterisks denote statistical significance (*$p < 0.05$, **$p < 0.01$, ***$p < 0.001$; two-sided tests).

3. Results

3.1. Neuromast distribution in three sinocyclocheilus species

The spatial distribution of neuromasts along the lateral line revealed clear differences among the three cavefish species (Figs. 2 and 3; Supplementary Fig. S6 and Table S3). Neuromast counts varied significantly among species across multiple body regions (Fig. 3). For the anterior region (head), CN counts differed between *S. grahami* and *S. rhinocerous* ($p = 0.0077$, $d = 2.62$), *S. grahami* and *S. furcodorsalis* ($p = 0.0053$, $d = -2.84$), and *S. rhinocerous* and *S. furcodorsalis* ($p = 0.0002$, $d = -5.46$); SN counts differed between *S. grahami* and *S. rhinocerous* ($p < 0.0001$, $d = 77.01$) and *S. grahami* and *S. furcodorsalis* ($p < 0.0001$, $d = 90.62$), while no significant difference was found between *S. rhinocerous* and *S. furcodorsalis* ($p = 0.4068$, $d = -0.70$). For the posterior part (trunk + tail), significant CN counts differed between *S. grahami* and *S. rhinocerous* ($p < 0.0001$, $d = 9.68$) and *S. grahami* and *S. furcodorsalis* ($p < 0.0001$, $d = 8.65$), but not between *S. rhinocerous* and *S. furcodorsalis* ($p = 0.8027$, $d = 0.18$); All comparisons showed significant differences in SNs ($p < 0.0001$, $d = 205.19, 111.16, -17.72$) among the species. For the caudal fin region, SNs showed significant differences for all pairwise comparisons, *S. grahami* vs. *S. rhinocerous* ($p < 0.0001$, $d = 28.29$), *S. grahami* vs. *S. furcodorsalis* ($p < 0.0001$, $d = 36.88$), and *S. rhinocerous* vs. *S. furcodorsalis* ($p = 0.0001$, $d = 9.47$). For the dorsal head region, CNs and SNs exhibited significant differences between *S. grahami* and *S. rhinocerous* ($p < 0.0001$, $d = 7.92$) as well as between *S. rhinocerous* and *S. furcodorsalis* ($p < 0.0001$, $d = -10.62$); No significant differences were noted for SNs between *S. grahami* and *S. furcodorsalis* ($p = 0.1084$, $d = 1.19$). For the ventral head region, CNs and SNs showed significant differences for all pairwise comparisons ($p < 0.0010$, $d = -4.04, -5.20, -1.15, -47.07, -108.11$, and -59.32), excluding CNs for *S. rhinocerous* vs. *S. furcodorsalis* ($p = 0.1340$, $d = -1.15$). For other regions, SNs also demonstrated significant differences among all species ($p < 0.0010$).

Consistent with the high energy cost of maintaining sensory organs in a nutrient-poor environment, the troglobitic cavefishes *S. rhinocerous* and *S. furcodorsalis* had significantly fewer SNs and CNs than the troglophilic *S. grahami* (Fig. 3). Specifically, the

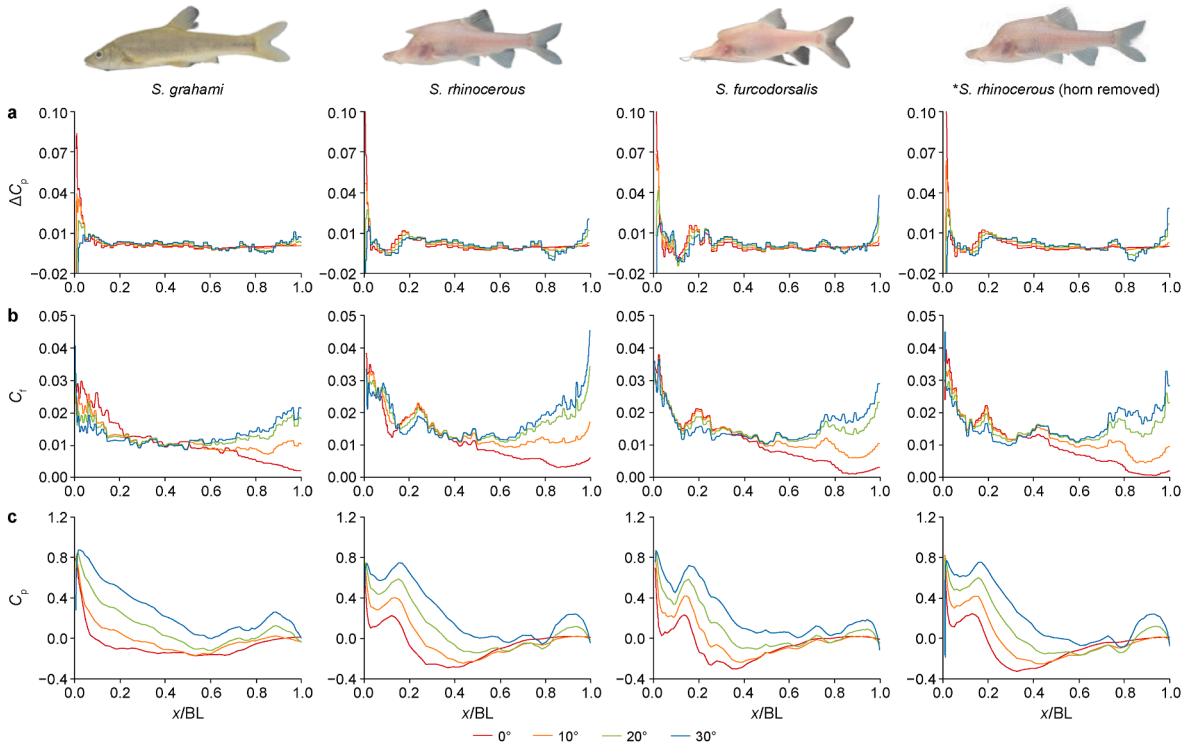

Fig. 4. Hydrodynamic stimuli along the cavefish body length during steady gliding in open water. Profiles are shown along the normalized body coordinate x/BL for four angles of attack ($\alpha = 0°$, 10°, 20°, and 30°) at Re $\approx 10^4$. **a**, Differential pressure coefficient (ΔC_p) used as a proxy for canal-neuromast (CN) stimulation, computed as the pressure difference between adjacent canal pores normalized by the dynamic pressure (kinetic energy per unit volume). **b**, Skin-friction coefficient (C_f) used as a proxy for superficial-neuromast (SN) stimulation, computed as wall shear stress normalized by the same dynamic pressure. **c**, Pressure coefficient (C_p) computed as surface pressure normalized by the dynamic pressure. x denotes location along the cavefish's surface. BL: body length.

number of SNs in *S. grahami* on the anterior part (head), posterior part (trunk + tail), caudal fin, and other regions (upper lateral line + dorsal fin base) was approximately 1.5, 2.6, 1.7, and 5.0 times greater, respectively, than in the two troglobitic species, while the number of CNs on the posterior part was around 1.5 times greater. The SNs were clustered on the lateral sides of the head (small green dots on the head, Fig. 2) in all three species. The distribution of SNs was more concentrated in the troglophilic cavefish *S. grahami*, while the two troglobitic cavefish displayed a relatively sparse arrangement, with the SNs being slightly denser on the head of *S. rhinocerous* than on *S. furcodorsalis*.

Within the anterior region (head), SNs were clustered in the vicinity of the regressed eyes (RE, Fig. 2) in *S. rhinocerous* and *S. furcodorsalis*, where CNs would normally be localized in the eyed *S. grahami*. While there were no neuromasts on the horn itself, SNs were concentrated along the bottom edge of the horn (HB, Fig. 2) in both *S. rhinocerous* and *S. furcodorsalis*.

In the posterior lateral line system, the distribution of CNs was almost identical across all three species, whereas SNs were uniformly distributed along both sides of the canal (Fig. 2). The number of CNs was slightly higher in *S. grahami* (Fig. 3). The distribution of SNs in *S. grahami* was broader than that observed in the two troglobitic cavefish species, and the distribution of SNs on the anterior trunk line of *S. furcodorsalis* exhibited some randomness. In the two troglobitic species, the diameter of the neuromasts and the number of hair cells were larger than those of the troglophilic species. This likely improves their perceptive ability and mechanosensation [43,44,70,71].

A series of SNs was also present on the upper lateral line (UL, Fig. 2) and the dorsal fin base (FB, Fig. 2) in all three species. Similar to the horn, no neuromasts were present on the hump. There were also no noticeable variations in the distribution of SNs in the caudal fins of the three species. Overall, the troglophilic *S. grahami* exhibited a higher number of SNs than the two troglobitic cavefish species.

As in the lateral view, the neuromast patterns on the head from dorsal and ventral sides (Supplementary Fig. S6) differed among species. On the ventral sides of the head, SNs were aligned along one pair of CNs for all three species, but the distribution of SNs in the two troglobitic cavefish was relatively sparse compared to the troglophilic cavefish. The distribution of neuromasts on the dorsal side of the head showed remarkable differences among species. A dense V-shaped arrangement of SNs characterized the dorsal head of *S. grahami*, while SNs were sparsely distributed across the entire dorsal head in *S. rhinocerous* and *S. furcodorsalis*.

In contrast to differences with SNs when viewed from the dorsal side, the CNs were embedded in the two canals on the dorsal sides of *S. grahami* and *S. furcodorsalis*. Notably, no CNs were detected on the dorsal sides of *S. rhinocerous* (Fig. 3 and Supplementary Fig. S6b), a finding that aligns with the observations reported by Chen et al. [56], who focused solely on the cephalic region of various *Sinocyclocheilus* species.

3.2. Enhanced hydrodynamic perception in troglobitic species

The pressure gradient and velocity signals received by lateral line neuromasts were influenced by the presence of the duckbilled head and hump, with the effect increasing with the increasing angle of attack (Fig. 4). ΔC_p quantifies the stimulus for the CNs (Fig. 4a) and C_f represents the stimulus for SNs (Fig. 4b). Although C_p (Fig. 4c) is not the direct signal detected by canal neuromasts, we also analyzed this additional parameter for reference, as

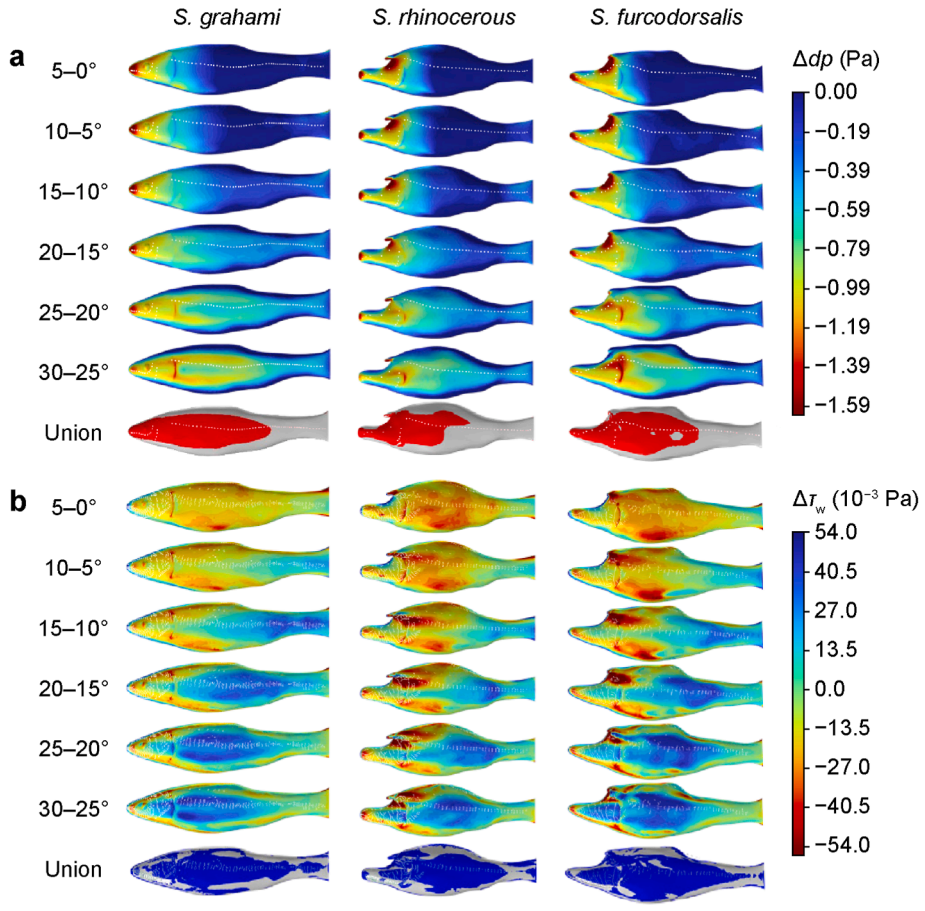

Fig. 5. Changes in lateral-surface hydrodynamic stimuli between adjacent angles of attack. Differences were computed between consecutive angles of attack (0–30°) during steady gliding in open water at Re ≈ 10^4. Columns correspond to the three species. **a**, Change in left–right differential pressure (Δdp) mapped on the lateral surface (proxy for canal-neuromast stimulation). **b**, Change in wall shear stress ($\Delta\tau_w$) mapped on the leeward lateral surface (proxy for superficial-neuromast stimulation). Bottom row, union of regions exhibiting pronounced changes across angle pairs ("Union"), shown for Δdp (red) and $\Delta\tau_w$ (blue), overlaid with the measured neuromast distributions for comparison.

reported in other studies [36,38,45,48,69]. Generally, a consistent pattern in ΔC_p, C_f, and C_p emerged, suggesting the influence of the duckbilled head and hump on the hydrodynamic stimuli along the lateral side of cavefish (Fig. 4).

In all three species, ΔC_p, C_f, and C_p started high and asymptotically approached zero as progressed from head to tail (Fig. 4). This pattern aligns with the observations made by Windsor et al. [48] and Ristroph et al. [69]. Notably, the specific morphological features of *S. rhinocerous* and *S. furcodorsalis* led to a 345.9% and 429.8% increase in ΔC_p, respectively, along with a 24.9% and 69.2% rise in C_f. Similarly, C_p increased by 123.5% and 651.4% in the same species. The significant signal amplification indicates a morphological adaptation that may compensate for the weak hydrodynamic cues available in the largely stagnant waters of karst aquifers. Furthermore, ΔC_p and C_f showed an upward trend with an attack angle of flow (α) after a relative body length of 0.8 and 0.5, respectively, while C_p increased with angle for a relative body length less than 0.5 (Fig. 4). The difference was the presence of a secondary peak in all ΔC_p, C_f, and C_p at a relative body length of approximately 0.2 for *S. rhinocerous* and *S. furcodorsalis* due to the second stagnation point occurring on the head. The similarity of the results for *S. rhinocerous* with and without the horn showed that the duckbilled head and hump, not the horn, are the primary drivers of the ΔC_p, C_f, and C_p differences with *S. grahami*.

The ΔC_p across the canal pores also serves as an indicator of perceptual range in all cavefish and was predominantly influenced by the presence of the duckbilled head and hump. Operationally, we define the perceptual range as the spatial domain along the body where ΔC_p exceeds a detectable threshold (>0). The duckbilled head and hump cause a secondary peak at a relative body length of about 0.2, which also provides some perception between 0.2 and 0.4, a range not present in *S. grahami* (Fig. 4a). The horn structure plays a distinct, localized role. It significantly enhances the pressure gradient signal received by CNs embedded on the dorsal side of the troglobitic cavefish head, the velocity stimulus sensed by SNs accumulated at the bottom edge of the horn (Supplementary Fig. S7b and d, and HB in Fig. 2b and c), and the dorsal part of the head (Supplementary Fig. S6b and c).

3.3. Remarkable variation of hydrodynamic stimulus

The pressure and wall shear stress distributed on the surface of the cavefish at an attack angle of 0° (Supplementary Fig. S7) reveal that the greatest stimuli are concentrated around the nose (and head horn) of the cavefish across all three studied species. We calculated Δdp and $\Delta\tau_w$ experienced on the surfaces of the three cavefish species (Fig. 5). These values were adjusted by subtracting the corresponding results from adjacent attack angles (larger minus smaller). The results indicated a pronounced concentration of differential pressure signals on the head across all three species, independent of how the attack angle changed, while (especially for small angles) the change in wall shear stress appeared on almost

the entire surface of the three species.

In the case of the two troglobitic species, a notable variation in differential pressure was detected on the lateral sides of the body as the attack angle increased (Fig. 5a). However, the greatest changes in differential pressure always remained in the vicinity of the horn. In the troglophilic species, a distinct region of differential pressure variation showed a gradual decrease from the head, which also shifted to the lateral sides with increasing attack angles. In terms of wall shear stress (Fig. 5b), changes occurred at the top and bottom sides of the cavefish surface at small attack angles and tended to move from tail to head with increasing attack angles. An area with a significant change in wall shear stress was maintained at the bottom edge of the horn in the two troglobitic cavefish, where there was intensive accumulation of SNs (HB in Fig. 2b and c).

The positions (with larger Δdp and $\Delta\tau_W$) corresponding to significant changes in hydrodynamic signals can be detected by combining regions with remarkably varied differential pressure and wall shear stress at all attack angles (Union in Fig. 5). The predicted regions of remarkable hydrodynamic variation showed a strong spatial correlation with the distribution of neuromast clusters, although there were some visible deviations, possibly due to the scanned morphological model used in CFD simulations, which differed somewhat from the actual cavefish shapes.

4. Discussion

The troglobitic cavefish *S. rhinocerous* and *S. furcodorsalis* inhabit a demanding ecological niche within karst aquifers, where perpetual darkness, stagnant flow, and severe energy constraints have driven the evolution of a specialized lateral line system. Our results reveal a strategy that balances these competing selective pressures: a reduction in neuromast numbers coupled with a morphological amplification of the signals reaching the remaining sensors.

The significantly fewer neuromasts in troglobitic species compared to the troglophilic *S. grahami* is consistent with an energy conservation strategy, as maintaining sensory organs is metabolically costly in nutrient-poor caves. This aligns with previous findings that troglobitic species rely more heavily on enhanced mechanosensory cues for navigation and prey detection in complete darkness [72,73]. However, the evolution of specialized structures such as the duckbilled head, horn, and hump provides a powerful compensatory mechanism. Our CFD models demonstrate that these features act as passive amplifiers, enhancing the pressure gradient signal available to canal neuromasts by up to 429.8% and the velocity-derived signal for superficial neuromasts by up to 69.2%. This suggests a sensory system optimization rather than a simple reduction, investing energy not in more sensors but in morphological features that dramatically increase the signal strength and perceptual range for each remaining sensor. The strong correlation between these amplified signal "hotspots" and neuromast clusters supports the functional integration of this strategy.

The varying morphology between these two troglobitic species further refines this principle. *S. rhinocerous* possesses a longer but thinner horn, which our models indicate results in lower stimulus amplification compared to *S. furcodorsalis*. This may help explain the subtle differences in their neuromast distributions and suggests that the evolution of lateral line neuromasts occurred independently across lineages in response to diverse selective pressures in different cave systems [56].

While our study demonstrates a primary role in enhancing hydrodynamic perception, the extreme morphologies of troglobitic *Sinocyclocheilus* likely confer composite advantages that improve survival in a resource-limited, three-dimensional cave environment. The amplified sensory "footprint" could increase foraging efficiency by enabling the detection of faint water movements from prey in largely stagnant pools. Similarly, an extended perceptual range may facilitate spatial mapping and earlier obstacle avoidance during navigation in total darkness. Beyond sensing, these structures may serve additional, nonexclusive functions. The dorsal hump, for instance, is a candidate site for adipose storage, providing an energy reserve to withstand the sporadic nutrient availability characteristic of karst aquifers [21]. The head horn may provide physical protection for the head during navigation through tight crevices or serve a social function [21]. Thus, the duckbilled head, horn, and hump may represent a complex multifaceted adaptive mechanism, with enhanced flow sensing as a central, but not sole, component of their evolutionary value.

The cavefish species we studied, *Sinocyclocheilus* (*S. grahami*, *S. rhinocerous*, and *S. furcodorsalis*), are found in karst cave systems in China (elevations up to 2700 m), where water flow is often low-velocity and stable, with turbulence due to irregular cave topography. For example, *S. rhinocerous* inhabits caves with

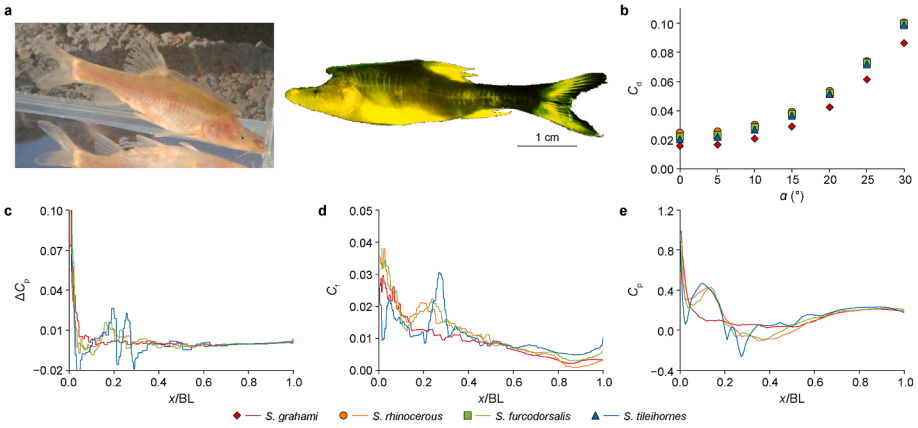

Fig. 6. Neuromasts distribution and hydrodynamic properties for *S. tileihornes*. **a**, Representative specimen photograph and vital staining showing neuromasts distribution alongside *S. grahami*, *S. rhinocerous*, and *S. furcodorsalis* for comparison. **b**, Dimensionless drag force (C_d) as a function of angle of attack (α) imposed on the cavefish body. **c**–**e**, Profiles along the normalized body coordinate *x*/BL of the differential pressure coefficient (ΔC_p, proxy for canal-neuromast stimulation, **c**), the skin-friction coefficient (C_f, proxy for superficial-neuromast stimulation, **d**), and the pressure coefficient (C_p, **e**). BL, body length. **c**, Pressure gradient signal (received by CNs) denoted as differential pressure coefficient ΔC_p. **d**, Velocity signal (received by SNs) denoted as skin friction coefficient C_f. **e**, Pressure applied on the cavefish's surface expressed by the pressure coefficient (C_p).

temperatures around 17.6 °C, a pH of 7.7, and dissolved oxygen levels lower than surface rivers, indicating an environment with relatively stable but nutrient-scarce conditions [74]. Several Chinese caves have lower flow rates, averaging around 2–3 $m^3\ s^{-1}$ annually, with peaks reaching 7–9 $m^3\ s^{-1}$ during the wet season and falling below 1 $m^3\ s^{-1}$ in the dry season, based on our field observations in 2017–2018 [74]. *S. rhinocerous*, and *S. furcodorsalis* inhabit caves with constant water temperatures and low flow, suggesting that the role of the lateral line in detecting small perturbations in water flow is essential for navigation and prey detection in a dark, nutrient-scarce environment.

The geographic distribution and diversification of *Sinocyclocheilus* cavefish are closely tied to the unique karst landscapes of southern China, shaped by the uplift of the Yunnan–Guizhou Plateau [19,75,76]. Troglobitic species (*S. rhinocerous* and *S. furcodorsalis*), primarily found in areas with steep slopes, rugged terrain, and laterally extensive subterranean systems, exhibit specialized morphology such as eye regression and duckbilled head, horn, and hump structures, likely developed in response to dark, oxygen-and-food-scarce, low-flow cave environments during periods of climatic instability, particularly the aridification of China in the late Miocene and Pliocene [76]. Troglophilic species (*S. grahami*) with fewer troglomorphic traits are more commonly associated with flatter topographies, such as the eastern Yunnan Plateau [75]. These spatially heterogeneous karst landscapes have played a key role in driving distinct ecological and morphological changes in *Sinocyclocheilus*.

The predicted variation of differential pressure and velocity signals from the CFD modeling basically covers the positions where the CNs and SNs accumulate, since only one situation is considered here—the gliding state of swimming cavefish at different angles of attack. In real-world situations involving attack angles, cavefish can detect and track prey by detecting flow changes analogous to dipole vibrations. Cavefish may also encounter complex flow conditions that are difficult to replicate in grid-based CFD models. We think that computational predictions of regions showing significant changes in response to stimuli would be consistent with the distribution of sensory organs. Therefore, it is possible to predict correlations between morphology, the lateral line system, and environmental shifts based on the present results.

To conceptually contextualize our findings within the broader morphological diversity of the genus, we consider the troglobitic *S. tileihornes* (Clade B: *angularis* group, same as *S. rhinocerous* and *S. furcodorsalis*), a species studied in prior work [38]. While the available neuromast distribution data for this species is less resolved than our primary dataset, its distinct tile-shaped horn provides an illustrative example. Even with this different morphology, the general principle holds: specialized structures alter the local flow field. This suggests that the evolution of morphology to modulate hydrodynamic stimuli is a recurring theme in *Sinocyclocheilus* adaptation, beyond the specific model series we quantitatively analyzed. A comprehensive phylogenetic analysis of these *Sinocyclocheilus* species is available in the literature [39,56]. Notably, the distribution of neuromasts in *S. tileihornes* differs markedly from that of *S. rhinocerous* and *S. furcodorsalis*. This distinction was evident in the broader and more sparsely distributed neuromasts in the posterior region (Fig. 6a) compared to the established patterns observed in the other two cavefish species. When we repeated our CFD analysis on the fourth species, we also predicted that its duckbilled head, horn, and hump structure would augment the hydrodynamic stimuli and that the regions with remarkable variations in signals would also be coincident with observed locations of neuromasts. Numerical modeling predicted greater elevated pressure gradient signals (ΔC_p increased from −0.008 to 0.023), enhanced velocity signals (C_f increased from 0.01 to 0.03), and larger pressure signal exposed on the cavefish's surface (C_p increased from −0.15 to 0.25) compared to the other two troglobitic cavefish species (Fig. 6c–e), even with a similar drag (Fig. 6b). This discrepancy is likely attributed to the specific morphological characteristics exhibited by *S. tileihornes*, which adds to the strength of our comparative approach and further confirms the role of the duckbilled head, horn, and hump that we predicted based on *S. rhinocerous* and *S. furcodorsalis*.

Despite morphological changes in troglobitic Chinese cavefish that increase flow resistance (Fig. 6b), they have gained heightened perception capabilities due to the enhanced hydrodynamic stimuli they receive. This adaptation may be related to reduced predator pressure in their cave habitats.

The sensory system plays a pivotal role in the autonomous manipulation, navigation, and imaging of underwater vehicles (e.g., AUVs). Currently, sonar is often used for navigation, object detection, and underwater imaging. However, sonar is energy-intensive, exhibits a near-field blind zone, and—despite its broad coverage—provides relatively low spatial resolution. Furthermore, there is a high risk that sonic signals will be easily detected by other equipment. Optical sensory systems can be incorporated into AUVs to compensate for the long-range imaging limitations of acoustic sensors, which perform better at shorter ranges, but light absorption and scattering effects often limit the practical use of optical sensors in extreme environments. Another sensor used for AUVs is the electromagnetic sensor, but it is also affected by environmental electromagnetic fields, which reduces precision [14].

In contrast, the lateral line system of cavefish enables hydrodynamic imaging that accurately maps the surrounding flow field through passive perception, effectively overcoming the limitations of conventional sensors [16]. For this reason, the lateral line system offers numerous advantages over traditional acoustic, optical, and electromagnetic sensor systems. Our finding that regions of significant hydrodynamic variation align with neuromast distribution provides a concrete biomimetic design principle for optimizing sensor placement in ALL systems. Nature employs a sophisticated “hotspots” strategy; sensory investment is not uniformly distributed but is strategically concentrated in bodily regions where inherent morphology actively amplifies and conditions ambient flow cues. This is a deliberate optimization of sensory resource allocation. Our analysis crystallizes this biological strategy into a two-tiered biomimetic framework for the engineering of bio-inspired hydrodynamic sensing arrays.

Tier 1 establishes morphology as a deterministic signal-processing layer. Through validated CFD modeling, we quantified the signal-enhancing function of specific troglobitic adaptations. The duckbilled head and dorsal hump act as integrated amplifiers, increasing the pressure gradient stimulus (ΔC_p) along the lateral body line by up to 429.8%. Concurrently, the horn structure functions as a flow director, creating a localized focus of high velocity signal (C_f) variation at its base. This is not a minor enhancement but a dramatic physical amplification of available environmental information. The engineering principle is clear and quantifiable: the hull of an underwater vehicle can be deliberately shaped to incorporate passive morphological features that preprocess hydrodynamic stimuli, thereby elevating the raw signal amplitude before it ever reaches a sensor. This principle directly addresses the core challenge of low-signal environments, offering a pathway to significantly boost sensor sensitivity and effective perceptual range without increasing power consumption.

Tier 2 defines a computational workflow for optimal sensor placement, moving from a principle to a practical design tool. The

biological "hotspot" map provides the optimization criterion, which we operationalize into a concrete, three-step engineering sequence. For any candidate hull geometry, which may inherently possess or be designed with Tier 1 enhancers, the first step is to perform a suite of CFD simulations. These simulations map the spatial distributions of Δdp and $\Delta\tau_w$ across a representative envelope of operational scenarios, including varying angles of attack and low ambient flow velocities characteristic of target environments. Second, the consolidated CFD datasets are then analyzed using computational algorithms. Techniques such as gradient-based peak detection or unsupervised clustering algorithms (e.g., *k*-means clustering applied to signal variance maps) can be employed to objectively identify and delineate discrete "hotspot" regions where hydrodynamic signal variation is consistently maximized. This algorithmic step ensures the design is rigorously performance-driven. Third, with hotspots defined, sensor integration follows a bio-inspired, heterogeneous strategy. Pressure-gradient sensors (analogous to CNs) are clustered in the identified Δdp hotspots, while flow-velocity sensors (analogous to SNs) are concentrated in $\Delta\tau_w$ hotspots. We further propose a graded sensor density strategy: maximizing density within these high-yield hotspots to fully capture the enhanced signals, while reducing density in areas of low predicted variation to optimize system-wide power, data bandwidth, and cost efficiency.

This integrated framework facilitates a paradigm shift from the conventional approach of attaching a uniform sensor grid to a predefined hull. Instead, it advocates co-design of the sensing platform, in which the vehicle's morphology and its sensor array are developed synergistically as an integrated perceptual system. The quantitative target from Tier 1 (e.g., >400% signal enhancement) provides a clear benchmark. It implies that sensors placed within engineered analogs of biological hotspots should, in principle, operate with a proportionally higher signal-to-noise ratio (SNR), offering a key metric for prototyping and benchmarking against conventional uniform arrays.

While the fabrication and field validation of full prototypes are the logical next steps, this study provides the essential missing link by offering foundational design principles, quantitative performance targets, and a concrete computational methodology, all derived from a successful biological model, to inform and accelerate that development. The proposed workflow offers a direct path to engineering ALL systems, specifically for the challenges of low-flow, turbid, and dark aquatic environments. Leveraging this framework, future sensor technologies, such as those enabled by advanced fabrication methods, such as laser direct writing [77–80], can be strategically integrated onto bionic robotic fish. Such systems, designed according to the observed principles of morphological amplification and optimal sensor placement, hold significant potential to overcome the limitations of existing AUVs, enabling persistent, energy-efficient, and high-resolution environmental monitoring in critical yet underserved aquatic ecosystems.

This study has inherent limitations that both contextualize our findings and highlight valuable directions for future research. Most significantly, the protected conservation status of the *Sinocyclocheilus* species precluded invasive or manipulative experiments. Consequently, direct molecular, neural, and behavioral validation of the modeled hydrodynamic function, such as genetic manipulation, electrophysiological recordings from neuromasts, or controlled behavioral assays of perceptual performance, was not feasible. Our approach, combining comparative morphology with computational fluid dynamics, was designed to extract maximal mechanistic insight using noninvasive, ethical methods. Similarly, the sample sizes for these rare species were constrained, although our statistical modeling accounts for individual variation. Similar to previous studies, our CFD framework employed standard steady-flow simplifications and fin exclusion to isolate the sensory role of core morphology. While direct experimental flow measurements around living specimens would offer valuable validation and verification against existing experimental data, the strong correlation between CFD-predicted signal hotspots and biological neuromast locations provides a compelling alternative line of evidence for the model's biological relevance.

To bridge the biological–engineering gap, the CFD-informed design principles derived here should be translated into functional prototypes. The next critical steps include: (1) fabrication and hydrodynamic validation of 3D-printed robotic fish embodying the amplifying morphologies, tested against PIV and pressure measurements in flow tanks; (2) sensor integration and benchmarking, embedding dense sensor arrays in the predicted hotspots to quantify performance gains in object detection and flow mapping compared to uniform arrays; and (3) closed-loop autonomy, integrating these optimized sensory skins into robotic fish or AUVs for testing in realistic, low-flow environments. This pathway from computational principle to physical system will test the real-world efficacy of the bio-inspired "hotspot" strategy and the quantitative performance targets (e.g., SNR improvement) for advanced environmental monitoring.

5. Conclusions

This study demonstrates how the unique morphological adaptations of Chinese cavefish in the genus *Sinocyclocheilus*, specifically the duckbilled head, dorsal horn, and hump, function as natural amplifiers of hydrodynamic stimuli, enhancing perception in dark, low-flow cave environments. By integrating neuromast distribution mapping with CFD simulations across a series of species (*S. grahami*, *S. rhinocerous*, and *S. furcodorsalis*), we show that these specialized structures significantly amplify differential pressure signals (by up to 429.8%) and velocity-derived signals (by up to 69.2%), while extending the perceptual range of the lateral line system. Importantly, we found a strong spatial correlation between regions of high hydrodynamic variation predicted by our models and the actual distribution of neuromasts, revealing a biologically optimized "hotspot" strategy for sensory placement.

These findings provide a biomimetic design framework for improving ALL systems in AUVs. The two-tiered approach proposed—Tier 1, using morphology as a passive signal amplifier, and Tier 2, employing CFD-driven hotspot detection for optimal sensor placement—offers a principled method to enhance sensor sensitivity, range, and energy efficiency in challenging aquatic environments. This work bridges evolutionary biology, fluid dynamics, and environmental engineering, offering a pathway toward more effective, bio-inspired monitoring technologies for data-scarce, turbid, and lightless underwater ecosystems.

Future efforts should focus on translating these principles into physical prototypes, integrating advanced sensor technologies, and validating performance in real-world conditions. By leveraging nature's evolutionary solutions, we can develop next-generation sensing systems capable of persistent, high-resolution environmental monitoring in some of the planet's most sensitive and inaccessible aquatic habitats.

CRediT authorship contribution statement

Qi Yang: Writing – original draft, Software, Methodology, Investigation, Formal analysis, Conceptualization. **Qirui Liu:** Writing – original draft, Methodology, Investigation, Formal analysis. **Yuling Wei:** Writing – original draft, Methodology, Investigation, Data curation. **Chubin Weng:** Writing – original draft,

Methodology, Investigation. **Li Ma:** Writing – review & editing, Validation, Supervision, Resources, Data curation. **He Tian:** Writing – review & editing, Validation, Data curation. **Fang Zhang:** Writing – review & editing, Validation, Data curation. **Kenneth A. Rose:** Writing – review & editing, Validation, Supervision. **William R. Jeffery:** Writing – review & editing, Validation, Supervision. **Mengzhen Xu:** Writing – review & editing, Validation, Supervision, Resources, Project administration, Funding acquisition, Conceptualization, Data curation.

Declaration of competing interest

The authors declare that they have no known competing financial interests or personal relationships that could have appeared to influence the work reported in this paper.

Acknowledgments

This work is financially supported by the National Natural Science Foundation of China (No. U2243222), Tsinghua University, China (No. 2022Z11QYJ044), National Key R&D Program of China (No. 2024YFA1803200), Yunnan Provincial Major Project for Basic Research (No. 202501BC070018) and Coordinate Innovation Center Projects (No. B2106019). We express our heartfelt gratitude to Zhao Rui, Chen Chunni, and Chen Huiqin for their valuable assistance with the vital staining experiments and to Zhu Boyi for his insights into bio-inspired sensors. Additionally, we extend our thanks to Prof. Mike Bisset, formerly of the Department of Physics at Tsinghua University, for his valuable discussions regarding the cavefish survey project.

Appendix. ASupplementary data

Supplementary data to this article can be found online at https://doi.org/10.1016/j.ese.2026.100677.

References

[1] G. Ioannou, N. Forti, L.M. Millefiori, et al., Underwater inspection and monitoring: technologies for autonomous operations, IEEE Aero. Electron. Syst. Mag. 39 (2024) 4–16.
[2] F. di Ciaccio, S. Troisi, Monitoring marine environments with autonomous underwater vehicles: a bibliometric analysis, Results Eng. 9 (2021) 100205.
[3] Z. Fan, J. Chen, J. Zou, D. Bullen, C. Liu, F. Delcomyn, Design and fabrication of artificial lateral line flow sensors, J. Micromech. Microeng. 12 (2002) 655.
[4] A.T. Abdulsadda, X. Tan, An artificial lateral line system using IPMC sensor arrays, Int. J. Smart Nano Mater. 3 (2012) 226–242.
[5] A. Klein, H. Bleckmann, Function of lateral line canal morphology, Integr. Zool. 10 (2015) 111–121.
[6] Y. Jiang, Z. Ma, D. Zhang, Flow field perception based on the fish lateral line system, Bioinspiration Biomimetics 14 (2019) 041001.
[7] Y. Zhai, X. Zheng, G. Xie, Fish lateral line inspired flow sensors and flow-aided control: a review, J. Bionic Eng. 18 (2021) 264–291.
[8] J. He, Y. Zhou, C. Zhang, et al., Online velocity estimation of a robotic fish using artificial lateral line system with velocity-decoupling sensing ability, IEEE Rob. Autom. Lett. 10 (2025) 10418–10425.
[9] Y. Zhai, X. Zheng, L.M. Chao, et al., An interpretable approach to estimate the self-motion in fish-like robots using mode decomposition analysis, Nat. Commun. 16 (2025) 3887.
[10] L. DeVries, D.A. Paley, Observability-based optimization for flow sensing and control of an underwater vehicle in a uniform flowfield, in: 2013 American Control Conference, IEEE, 2013, pp. 1386–1391.
[11] A. Ahrari, H. Lei, M.A. Sharif, K. Deb, X. Tan, Reliable underwater dipole source characterization in 3D space by an optimally designed artificial lateral line system, Bioinspiration Biomimetics 12 (2017) 036010.
[12] S. Verma, C. Papadimitriou, N. Lüthen, G. Arampatzis, P. Koumoutsakos, Optimal sensor placement for artificial swimmers, J. Fluid Mech. 884 (2020) A24.
[13] Y. Jiang, Z. Gong, Z. Yang, et al., Underwater source localization using an artificial lateral line system with pressure and flow velocity sensor fusion, IEEE ASME Trans. Mechatron. 27 (2022) 245–255.
[14] Z. Wang, S. Wang, X. Wang, X. Luo, Underwater moving object detection using superficial electromagnetic flow velocimeter array-based artificial lateral line system, IEEE Sens. J. 24 (2024) 12104–12121.
[15] T. Fu, Q. Hu, G. Jiang, J. Zhao, L. Shan, Underwater source localization using a distributed composite artificial lateral line system with pressure and active electric sensing fusion, Mech. Syst. Signal Process. 223 (2025) 111904.
[16] L. Ma, Y.H. Zhao, J.X. Yang, Cavefish of China, in: W.B. White, D.C. Culver, T. Pipan (Eds.), Encyclopedia of Caves, third ed., Academic Press, Waltham, 2019, pp. 237–254.
[17] L. Li, X. Fan, G. Chen, et al., From fish to fiber: 3D-Nanoprinted optical neuromast for multi-integrated underwater detection, Nat. Commun. 16 (2025) 7390.
[18] M.S. Triantafyllou, G.D. Weymouth, J. Miao, Biomimetic survival hydrodynamics and flow sensing, Annu. Rev. Fluid Mech. 48 (2016) 1–24.
[19] T.L. Poulson, W.B. White, The cave environment, Science 165 (1969) 971–981.
[20] Y. Zhao, R.E. Gozlan, C. Zhang, Out of sight out of mind: current knowledge of Chinese cave fishes, J. Fish. Biol. 79 (2011) 1545–1562.
[21] J.X. Yang, X.L. Chen, J. Bai, et al., The *Sinocyclocheilus* cavefish genome provides insights into cave adaptation, BMC Biol. 14 (2016) 1–13.
[22] M.L. Niemiller, M.E. Bichuette, P. Chakrabarty, et al., Cavefishes, in: W.B. White, D.C. Culver, T. Pipan (Eds.), Encyclopedia of Caves, third ed., Academic Press, Waltham, 2019, pp. 227–236.
[23] R.L. Moran, E.J. Richards, C.P. Ornelas-García, et al., Selection-driven trait loss in independently evolved cavefish populations, Nat. Commun. 14 (2023) 2557.
[24] T. Teyke, Morphological differences in neuromasts of the blind cavefish *Astyanax hubbsi* and the sighted river fish *Astyanax mexicanus*, Brain Behav. Evol. 35 (1990) 23–30.
[25] Y. Yamamoto, W.R. Jeffery, Central role for the lens in cave fish eye degeneration, Science 289 (2000) 631–633.
[26] Y. Yamamoto, D.W. Stock, W.R. Jeffery, Hedgehog signalling controls eye degeneration in blind cavefish, Nature 431 (2004) 844–847.
[27] E.R. Duboué, A.C. Keene, R.L. Borowsky, Evolutionary convergence of sleep loss in cavefish, Curr. Biol. 21 (2011) 671–676.
[28] J.E. Kowalko, N. Rohner, T.A. Linden, et al., Convergence in feeding posture occurs through different genetic loci in independently evolved cave populations of *Astyanax mexicanus*, Proc. Natl. Acad. Sci. USA 110 (2013) 16933–16938.
[29] Y. Elipot, H. Hinaux, J. Callebert, et al., A mutation in the enzyme monoamine oxidase explains part of the *Astyanax cavefish* behavioral syndrome, Nat. Commun. 5 (2014) 3647.
[30] M. Riddle, A. Aspiras, K. Gaudenz, et al., Insulin resistance in cavefish as an adaptation to a nutrient-limited environment, Nature 555 (2018) 647–651.
[31] C. Hyacinthe, J. Attia, S. Rétaux, Evolution of acoustic communication in blind cavefish, Nat. Commun. 10 (2019) 4231.
[32] K. Pottin, C. Hyacinthe, S. Rétaux, Conservation, development, and function of a cement gland-like structure in the fish *Astyanax mexicanus*, Proc. Natl. Acad. Sci. USA 107 (2010) 17256–17261.
[33] M.E. Protas, P. Trontelj, N.H. Patel, Genetic basis of eye and pigment loss in the cave crustacean, *Asellus aquaticus*, Proc. Natl. Acad. Sci. USA 108 (2011) 5702–5707.
[34] N. Rohner, The cavefish Astyanax mexicanus, Nat. Methods 20 (2023) 948–950.
[35] A. Tripathy, M.J. Nine, D. Losic, F.S. Silva, Nature inspired emerging sensing technology: recent progress and perspectives, Mater. Sci. Eng. R Rep. 146 (2021) 100647.
[36] Z. Yang, Z. Gong, Y. Jiang, et al., Maximized hydrodynamic stimulation strategy for placement of differential pressure and velocity sensors in artificial lateral line Systems, IEEE Rob. Autom. Lett. 7 (2022) 2170–2177.
[37] Z. Zhao, Q. Yang, R. Li, et al., A comprehensive review on the evolution of bio-inspired sensors from aquatic creatures, Cell Rep. Phys. Sci. 5 (2024) 102064.
[38] F. Lei, M. Xu, Z. Ji, et al., Swimming behavior and hydrodynamics of the Chinese cavefish *Sinocyclocheilus rhinocerous* and a possible role of its head horn structure, PLoS One 17 (2022) e0270967.
[39] T. Mao, Y. Liu, M.M. Vasconcellos, et al., Evolving in the darkness: phylogenomics of *Sinocyclocheilus* cavefishes highlights recent diversification and cryptic diversity, Mol. Phylogenet. Evol. 168 (2022) 107400.
[40] J.F. Webb, Morphological diversity, development, and evolution of the mechanosensory lateral line system, in: S. Coombs, H. Bleckmann, R.R. Fay, A.N. Popper (Eds.), The Lateral Line System, Springer, New York, 2014, pp. 17–72.
[41] M. Yoshizawa, W.R. Jeffery, S.M. van Netten, M.J. McHenry, The sensitivity of lateral line receptors and their role in the behavior of Mexican blind cavefish (*Astyanax mexicanus*), J. Exp. Biol. 217 (2014) 886–895.
[42] M. Protas, W.R. Jeffery, Evolution and development in cave animals: from fish to crustaceans, Wiley Interdiscip. Rev. Dev. Biol. 1 (2012) 823–845.
[43] Y. Jiang, J. Fu, D. Zhang, Y. Zhao, Investigation on the lateral line systems of 2 cave fish: *sinocyclocheilus macrophthalmus* and *S. microphthalmus* (Cypriniformes: cyprinidae), J. Bionic Eng. 13 (2016) 108–114.
[44] Z. Ma, Y. Jiang, Z. Dong, et al., Hydrodynamic perception using an artificial lateral line device with an optimized constriction canal, J. Bionic Eng. 17 (2020) 909–919.
[45] Z. Ma, Z. Gong, Y. Jiang, et al., Head horn enhances hydrodynamic perception in eyeless cavefish, Adv. Sci. 11 (2024) 2406707.
[46] C.F. Baker, J.C. Montgomery, The sensory basis of rheotaxis in the blind Mexican cave fish, *Astyanax fasciatus*, J. Comp. Physiol. 184 (1999) 519–527.
[47] A. Ghysen, C. Dambly-Chaudière, The lateral line microcosmos, Genes Dev. 21

(2007) 2118–2130.
[48] S.P. Windsor, S. Norris, S.M. Cameron, et al., The flow fields involved in hydrodynamic imaging by blind Mexican cave fish (*Astyanax fasciatus*). Part I: open water and heading towards a wall, J. Exp. Biol. 213 (2010) 3819–3831.
[49] K. Sumi, R. Asaoka, M. Nakae, K. Sasaki, Innervation of the lateral line system in the blind cave-fish *Astyanax mexicanus* (Characidae) and comparisons with the eyed surface dwelling form, Ichthyol. Res. 62 (2015) 420–430.
[50] E. Lloyd, C. Olive, B.A. Stahl, et al., Evolutionary shift towards lateral line dependent prey capture behavior in the blind Mexican cavefish, Dev. Biol. 441 (2018) 328–337.
[51] E.T. Lunsford, A. Paz, A.C. Keene, J.C. Liao, Evolutionary convergence of a neural mechanism in the cavefish lateral line system, eLife 11 (2022) e77387.
[52] L. Espinasa, R. Diamant, E. Vinepinsky, M. Espinasa, Evolutionary modifications of *Astyanax* larval prey capture (LPC) in a dark environment, Zool. Res. 44 (2023) 750–760.
[53] M.L. Niemiller, B.M. Fitzpatrick, P. Shah, et al., Evidence for repeated loss of selective constraint in rhodopsin of amblyopsid cavefishes (Teleostei: amblyopsidae), Evolution 67 (2013) 732–748.
[54] E. Trajano, M.E. Bichuette, Subterranean fishes of Brazil, in: E. Trajano, M.E. Bichuette, B.G. Kapoor (Eds.), The Biology of Subterranean Fishes, Science Publ., Boca raton, 2010, pp. 331–354.
[55] Z. Ma, H. Herzog, Y. Jiang, et al., Exquisite structure of the lateral line system in eyeless cavefish *Sinocyclocheilus tianlinensis* contrasts with eyed *Sinocyclocheilus macrophthalmus* (Cypriniformes: Cyprinidae), Integr. Zool. 15 (2020) 314–328.
[56] B. Chen, T. Mao, Y. Liu, et al., Sensory evolution in a cavefish radiation: patterns of neuromast distribution and associated behavior in *Sinocyclocheilus* (Cypriniformes: cyprinidae), Proc. R. Soc. A B 289 (2022) 20221641.
[57] M.S. Triantafyllou, G.S. Triantafyllou, D.K.P. Yue, Hydrodynamics of fishlike swimming, Annu. Rev. Fluid Mech. 32 (2000) 33–53.
[58] J.K. Shang, H.A. Stone, A.J. Smits, Vortex and structural dynamics of a flexible cylinder in cross-flow, Phys. Fluids 26 (2014) 053605.
[59] J.K. Shang, Flexibility and Curvature Effects on Vortex Dynamics and fluid-structure Interactions, Princeton University, 2015. Ph.D. thesis.
[60] J.K. Shang, H.A. Stone, A.J. Smits, Flow past finite cylinders of constant curvature, J. Fluid Mech. 837 (2018) 896–915.
[61] H.K. Versteeg, W. Malalasekera, An Introduction to Computational Fluid Dynamics: the Finite Volume Method, second ed., Pearson, Harlow, 2007.
[62] F.R. Menter, Two-equation eddy-viscosity turbulence models for engineering applications, AIAA J. 32 (1994) 1598–1605.
[63] D. Mateescu, M. Abdo, Aerodynamic analysis of airfoils at very low reynolds numbers, in: 42nd AIAA Aerospace Sciences Meeting and Exhibit, Reston, NV, 2004, pp. 6341–6351.
[64] T. Lutz, W. Wurz, S. Wagner, Numerical optimization and wind tunnel testing of low Reynolds-number airfoils, in: T.J. Mueller (Ed.), Fixed and Flapping Wing Aerodynamics for Micro Air Vehicles Applications, AIAA, Reston, 2001, pp. 169–190.
[65] N. Gregory, C.L. O'Reilly, Low-speed aerodynamic characteristics of NACA0012 aerofoil sections, including the effects of upper-surface roughness simulation hoar frost, Rep. Memoranda 3726 (1970).
[66] P. Moin, T.H. Shih, D.M. Driver, N.N. Mansour, Direct numerical simulation of a three-dimensional turbulent boundary layer, Phys. Fluids 2 (1990) 1846–1853.
[67] M.A. Rapo, H. Jiang, M.A. Grosenbaugh, S. Coombs, Using computational fluid dynamics to calculate the stimulus to the lateral line of a fish in still water, J. Exp. Biol. 212 (2009) 1494–1505.
[68] S.P. Windsor, M.J. McHenry, The influence of viscous hydrodynamics on the fish lateral-line system, Integr. Comp. Biol. 49 (2009) 691–701.
[69] L. Ristroph, J.C. Liao, J. Zhang, Lateral line layout correlates with the differential hydrodynamic pressure on swimming fish, Phys. Rev. Lett. 114 (2015) 018102.
[70] Y. Jiang, Z. Ma, J. Fu, D. Zhang, Development of a flexible artificial lateral line canal system for hydrodynamic pressure detection, Sensors 17 (2017) 1220.
[71] D. Soares, M.L. Niemiller, Sensory adaptations of fishes to subterranean environments, Bioscience 63 (2013) 274–283.
[72] A. Romero, S.M. Green, The end of regressive evolution: examining and interpreting the evidence from cave fishes, J. Fish. Biol. 67 (2005) 3–32.
[73] M. Yoshizawa, Š. Goricki, D. Soares, W.R. Jeffery, Evolution of a behavioral shift mediated by superficial neuromasts helps cavefish find food in darkness, Curr. Biol. 20 (2010) 1631–1636.
[74] F. Lei, Characteristics and Conservation of the Chinese *Sinocyclocheilus* Cavefish's Aquatic Habitat, Tsinghua University, 2021. Ph.D. thesis.
[75] H. Xiao, S. Chen, Z. Liu, et al., Molecular phylogeny of *sinocyclocheilus* (Cypriniformes: cyprinidae) inferred from mitochondrial DNA sequences, Mol. Phylogenet. Evol. 36 (2005) 67–77.
[76] T.R. Mao, Y.W. Liu, M. Meegaskumbura, et al., Evolution in *Sinocyclocheilus* cavefish is marked by rate shifts, reversals, and origin of novel traits, BMC Ecol. Evol. 21 (2021) 45.
[77] L. Tao, H. Tian, Y. Liu, et al., An intelligent artificial throat with sound-sensing ability based on laser induced graphene, Nat. Commun. 8 (2017) 14579.
[78] F. Wu, H. Tian, Y. Shen, et al., Vertical MoS_2 transistors with sub-1-nm gate lengths, Nature 603 (2022) 259–264.
[79] H. Tian, X. Li, Y. Wei, et al., Bioinspired dual-channel speech recognition using graphene-based electromyographic and mechanical sensors, Cell Rep. Phys. Sci. 3 (2022) 101075.
[80] H. Tian, X. Li, G. Gou, et al., Graphene-based two-stage enhancement pressure sensor for subtle mechanical force monitoring, ACS Appl. Mater. Interfaces 16 (2023) 1005–1014.